

Measuring out-of-time-order correlators on a nuclear magnetic resonance quantum simulator

Jun Li,¹ Ruihua Fan,^{2,3} Hengyan Wang,⁴ Bingtian Ye,³ Bei Zeng,^{5,6,2,*} Hui Zhai,^{2,†} Xinhua Peng,^{4,7,8,‡} and Jiangfeng Du^{4,7}

¹*Beijing Computational Science Research Center, Beijing, 100094, China*

²*Institute for Advanced Study, Tsinghua University, Beijing, 100084, China*

³*Department of Physics, Peking University, Beijing, 100871, China*

⁴*Hefei National Laboratory for Physical Sciences at Microscale and Department of Modern Physics, University of Science and Technology of China, Hefei, Anhui 230026, China*

⁵*Department of Mathematics & Statistics, University of Guelph, Guelph N1G 2W1, Ontario, Canada*

⁶*Institute for Quantum Computing, University of Waterloo, Waterloo N2L 3G1, Ontario, Canada*

⁷*Synergetic Innovation Center of Quantum Information and Quantum Physics, University of Science and Technology of China, Hefei, Anhui 230026, China*

⁸*College of Physics and Electronic Science, Hubei Normal University, Huangshi, Hubei 435002, China*

The idea of out-of-time-order correlator (OTOC) has recently emerged in the study of both condensed matter and gravity systems. It not only plays a key role in investigating the holographic duality between a strongly interacting quantum system and a gravity system, but also diagnoses the chaotic behavior of many-body quantum systems and characterizes the information scrambling [1–6]. Based on OTOCs, three different concepts – quantum chaos, holographic duality, and information scrambling – are found to be intimately related to each other. Here we report the measurement of OTOCs of an Ising spin chain on a nuclear magnetic resonance (NMR) quantum simulator. We observe that the OTOC behaves differently in the integrable and chaotic cases [6]. Based on the recent discovered relationship between OTOCs and the growth of entanglement entropy in the many-body system [7], we extract the entanglement entropy from the measured OTOCs, which clearly shows that the information entropy oscillates in time for integrable models and scrambles for chaotic models [6]. With OTOCs, we also obtain the butterfly velocity in this system, which measures the speed of correlation propagation [5, 6, 8–10]. Our experiment paves a way for experimental studying holographic duality, quantum chaos, and information scrambling in many-body quantum systems with quantum simulators.

The out-of-time-order correlator (OTOC), given by

$$F(t) = \langle \hat{B}^\dagger(t) \hat{A}^\dagger(0) \hat{B}(t) \hat{A}(0) \rangle_\beta, \quad (1)$$

is a quantum generalization of a classical measure of chaos [1, 2]. Here \hat{H} is the system Hamiltonian and $\hat{B}(t) = e^{i\hat{H}t} \hat{B} e^{-i\hat{H}t}$, and $\langle \dots \rangle_\beta$ denotes averaging over a thermal ensemble at temperature $1/\beta = k_B T$. For a many-body system with local operators \hat{A} and \hat{B} , the exponential deviation from unity of a normalized OTOC

gives rise to the Lyapunov exponent λ_L , i.e. $F(t) \sim 1 - \#e^{\lambda_L t}$ for small t .

In the recent years, the interests on the OTOCs increase significantly. It is found that OTOC emerges in describing a bulk scattering nearby the horizon and information scrambling of a black hole [3–5]. Furthermore, quantum systems holographic dual to a black hole saturate an upper bound $2\pi/\beta$ of the Lyapunov exponent λ_L [11–15]. This establishes a profound connection between the existence of holographic duality and the chaotic behavior in many-body quantum systems. Recent studies also reveal that the OTOC can be applied to study physical properties beyond chaotic systems, for instance, to characterize many-body localized phases, which are not even thermalized [7, 16–19]. In the high temperature limit (i.e. $\beta = 0$), intimate connection between the OTOC and the growth of entanglement entropy in quantum many-body systems are also established [6, 7].

Despite of the significance of the OTOC revealed by recent theories, experimental measurement of the OTOC remains challenging. Unlike the normal correlators, the OTOC cannot be related to conventional spectroscopy measurements through linear response theory. Recently, several theory proposals have been put forward to measure OTOC, using echo- and interferometric- approaches [20–23].

Since the OTOC involves system dynamics and its time reversal, quantum computers provide an ideal platform to simulate these systems and their dynamics [24]. Historically, one of the key motivation to develop quantum computers is to simulate the dynamics of many-body quantum systems [25]. Quantum simulation of many-body dynamics has been theoretically shown to be efficient with practical algorithms proposed [26], and experimentally implemented in various kinds of quantum systems [27–29].

In this work, we report measurements of OTOCs on a NMR quantum simulator. The system to simulate is an

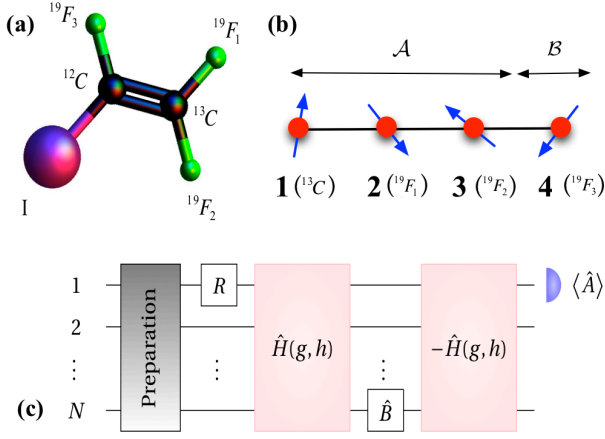


FIG. 1: Illustration of the Physical System and the Model: (a) The C_2F_3I molecule used in the NMB simulation. (b) The four sites Ising spin chain, \mathcal{A} and \mathcal{B} label dividing the entire system into two subsystems in the later discussion of entanglement entropy. (c) Experimental circuit for measuring the OTOC when $\beta = 0$. Here $R = \mathbf{1}, \hat{R}_x(-\frac{\pi}{2}), \hat{R}_y(\frac{\pi}{2})$ for $\hat{A} = \hat{\sigma}_1^z, \sigma_1^y, \sigma_1^x$, respectively.

Ising spin chain model, whose Hamiltonian is written as

$$\hat{H} = \sum_i (-\hat{\sigma}_i^z \hat{\sigma}_{i+1}^z + g \hat{\sigma}_i^x + h \hat{\sigma}_i^z), \quad (2)$$

where $\sigma_i^{x,y,z}$ are Pauli matrices on the i -site. The parameter values $g = 1, h = 0$ correspond to the transverse field Ising model, where the system is integrable. The system is non-integrable whenever both g and h are non-zero. We simulate the dynamics governed by the system Hamiltonian \hat{H} , and measure the OTOCs of operators that are initially acting on different local sites. The time dynamics of OTOCs is observed, from which entanglement entropy of the system and butterfly velocities of the chaotic systems are extracted.

NMR Quantum Simulator. The physical system to perform the quantum simulation is the nuclear spins in the molecules of Iodotrifluoroethylene (C_2F_3I) dissolved in d-chloroform [30], whose molecular structure is shown in Fig. 1(a). One ^{13}C nucleus and three ^{19}F nuclei ($^{19}F_1, ^{19}F_2$ and $^{19}F_3$) in the molecule consist of a four-qubit quantum simulator, taking the role as four spin sites of the Ising chain, respectively, as shown in Fig. 1(b).

The natural Hamiltonian of the physical system in a static magnetic field is

$$\hat{H}_{NMR} = -\sum_{i=1}^4 \frac{\omega_{0i}}{2} \hat{\sigma}_i^z + \sum_{i<j,=1}^4 \frac{\pi J_{ij}}{2} \hat{\sigma}_i^z \hat{\sigma}_j^z, \quad (3)$$

which is different from the Ising spin chain model in Eq. (2). The experiments were carried out at the Bruker AV-400MHz spectrometer (9.4T) at room temperature $T = 300K$. Here ω_{0i} represents the Larmor frequency of

spin i and J_{ij} the coupling constants, whose measured values are listed in the Supplementary Information.

The system is originally in the thermal equilibrium state populated according to the Boltzmann distribution. In high-temperature approximation, $\hat{\rho}_{eq} \approx 1/2^4 (\mathbf{1} + \sum_{i=1}^4 \epsilon_i \hat{\sigma}_i^z)$, where $\mathbf{1}$ is the identity and $\epsilon_i \sim 10^{-5}$ denotes the equilibrium polarization of spin i . Because there is no observable and dynamical effect on $\mathbf{1}$, $\hat{\rho}_{eq} \propto \sum_{i=1}^4 \epsilon_i \hat{\sigma}_i^z$.

The spins can be manipulated by applying an electromagnetic field which rotates in the x - y plane at ω_{rf} , at or near the Larmor frequency ω_{0i} : $\hat{H}_{rf} = -\sum_{i=1}^4 \frac{\omega_{1i}}{2} [\cos(\omega_{rf}t + \phi) \hat{\sigma}_i^x - \sin(\omega_{rf}t + \phi) \hat{\sigma}_i^y]$, where ϕ is the phase of the RF field, and ω_{1i} the Rabi frequency of spin i . This system has been demonstrated complete controllability [31, 32], which guarantees that one can simulate the dynamics of any other four-qubit system.

Using the Trotter formula [33, 34], the time evolution $e^{-i\hat{H}t}$ of the Ising spin chain of Eq. (2) can be approximately simulated by piecewise applications of local Hamiltonians, namely,

$$e^{-i\hat{H}m\tau} \approx \left(e^{-i\hat{H}_x \frac{\tau}{2}} e^{-i\hat{H}_z \frac{\tau}{2}} e^{-i\hat{H}_{zz}\tau} e^{-i\hat{H}_z \frac{\tau}{2}} e^{-i\hat{H}_x \frac{\tau}{2}} \right)^m$$

for small enough τ , with $\hat{H}_x = \sum_i g \hat{\sigma}_i^x$, $\hat{H}_z = \sum_i h \hat{\sigma}_i^z$ and $\hat{H}_{zz} = \sum_i -\hat{\sigma}_i^z \hat{\sigma}_{i+1}^z$. Likewise, the reversal of Ising dynamics can be implemented by a similar technique (see Methods for details).

Measuring OTOC. The OTOC can directly be obtained by measuring the expectation value of the observable $\hat{O} = e^{i\hat{H}t} \hat{B} e^{-i\hat{H}t} \hat{A} e^{i\hat{H}t} \hat{B} e^{-i\hat{H}t} \hat{A}$. For the infinite temperature $\beta = 0$, the equilibrium state of the many-body system \hat{H} is the maximally mixed state $\mathbf{1}/2^N$. When \hat{B} is unitary, the OTOC is measured by

$$\langle \hat{O} \rangle_{\beta=0} = \text{Tr}[\rho(t) \hat{A}] = \text{Tr} \left(\hat{U}(t) \hat{\rho}_0 \hat{U}^\dagger(t) \hat{A} \right), \quad (4)$$

where $\hat{U}(t) = e^{i\hat{H}t} \hat{B} e^{-i\hat{H}t}$ and $\rho_0 \propto \hat{\mathbf{1}}$. The general protocol for measuring OTOC for $\beta = 0$ is illustrated in Fig. 1(c). In the experiments, we chose different pairs of \hat{A} and \hat{B} from the set $\left\{ \hat{A} = \hat{\sigma}_1^\alpha, \hat{B} = \hat{\sigma}_4^\gamma : \alpha, \gamma = x, y, z \right\}$.

Two sets of typical experimental results of the OTOC at $\beta = 0$ are shown in Fig. 2. Here we normalize the OTOC by $\langle \hat{B}^\dagger(0) \hat{B}(0) \rangle \langle \hat{A}^\dagger(0) \hat{A}(0) \rangle$, and because \hat{A} and \hat{B}^\dagger commute at $t = 0$, the initial value of this normalized OTOC is unity. The experimental data (red points) agree very well with the theoretical results (blue curves). We also measure OTOC for other operators ($\hat{A} = \hat{\sigma}_1^\alpha, \hat{B} = \hat{\sigma}_4^\gamma$ with $\alpha, \gamma = x, y, z$) and they all behave similarly (see Supplementary Information).

In both the integrable case (the first column) and the chaotic cases (the second and the third columns), the early time behaviors look similar. That is, the OTOC

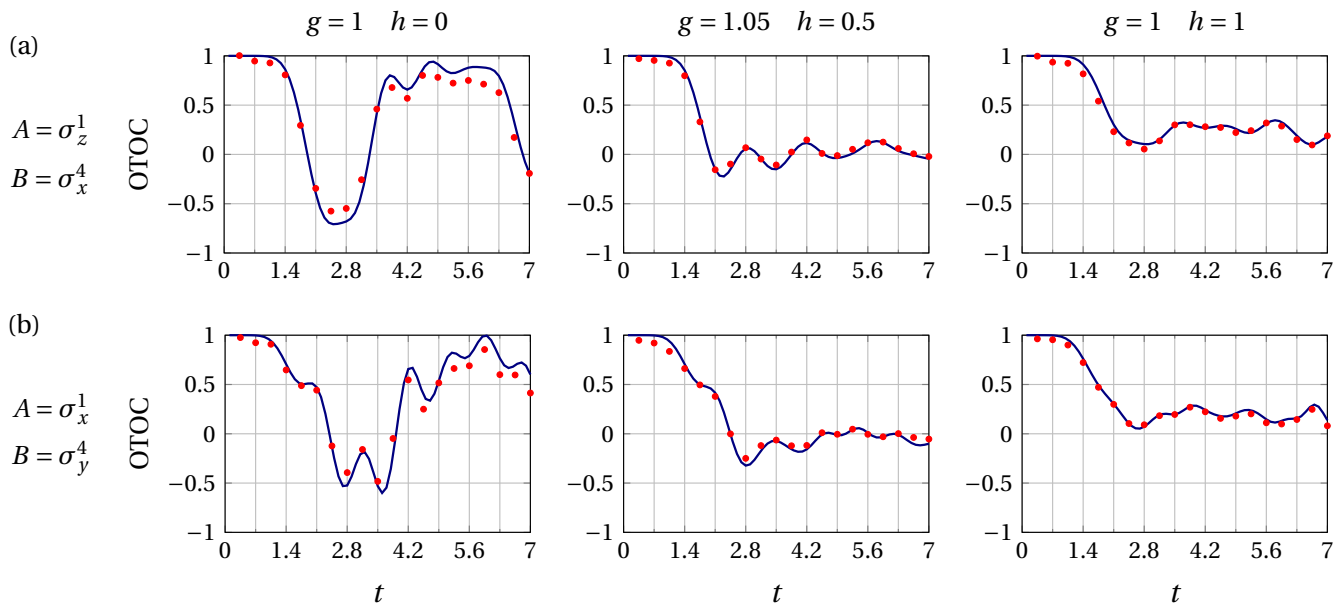


FIG. 2: Experimental Results of OTOC for an Ising Spin Chain: (a) $\hat{A} = \hat{\sigma}_1^z$ at the first site, and $\hat{B} = \hat{\sigma}_4^x$ at the fourth site. (b) $\hat{A} = \hat{\sigma}_1^x$ at the first site, and $\hat{B} = \hat{\sigma}_4^y$ at the fourth site. The three columns correspond to $g = 1, h = 0$; $g = 1.05, h = 0.5$; and $g = 1, h = 1$ of model Eq. (2), respectively. The red points are experimental data, the blue curves are theoretical calculation of OTOC with model Eq. (2) for four sites.

starts to deviate from unity after a certain time. However, the long time behaviors are very different between the integrable and chaotic cases. In the integrable case, after the decreasing period, the OTOC revives and recovers unity. This reflects that the system has well-defined quasi-particle. And there exists extensive number of integral of motions, which is related to the fact that an integrable system does not thermalize. While in the chaotic case, the OTOC decreases to a small value and oscillates, which will not revive back to unity in a practical time scale. This relates to the fact that the information does scramble in a chaotic system [6].

Entanglement Entropy. To better illustrate the different behaviors of the information dynamics in the two cases of integrable and chaotic systems, we reconstruct the entanglement entropy of a subsystem from the measured OTOCs. Entanglement entropy has become an important quantity not only for quantum information processing, but also for describing a quantum many-body system, such as quantum phase transition, topological order and thermalization [35]. However, measuring entanglement entropy is always challenging [36, 37] and so far is limited to few cases [38–41].

OTOC opens a new door for entanglement entropy measurement. An equivalence relationship between OTOCs at equilibrium and the growth of the 2nd Rényi entropy after a quench has recently been established [7], which states that

$$\exp(-S_{\mathcal{A}}^{(2)}) = \sum_{\hat{M} \in \mathcal{B}} \langle \hat{M}(t) \hat{V}(0) \hat{M}(t) \hat{V}(0) \rangle_{\beta=0}. \quad (5)$$

In the left-hand side of Eq. (5), $S_{\mathcal{A}}^{(2)}$ is the 2nd Rényi entropy of the subsystem \mathcal{A} , after the system is quenched by an operator \hat{O} at time $t = 0$. That is, $S_{\mathcal{A}}^{(2)} = -\log \rho_{\mathcal{A}}^2$ and $\rho_{\mathcal{A}} = \text{Tr}_{\mathcal{B}}(e^{-i\hat{H}t} \hat{V} e^{i\hat{H}t})$, and $\hat{V} = \hat{O} \hat{O}^\dagger$, up to a certain normalization condition (see Supplementary Information). The right-hand side of Eq. (5) is a summation over OTOCs at equilibrium. \hat{M} is a complete set of operators in the subsystem \mathcal{B} .

In our experiment, we choose the quench operator $\hat{O} \propto (\mathbf{1} + \hat{\sigma}_1^x)$ at the first site, and we take the first three sites as the subsystem \mathcal{A} and the fourth site as the subsystem \mathcal{B} , as marked in Fig. 1(b). In this setting, $S_{\mathcal{A}}^{(2)}$ measures how much the quench operation induces additional correlation between the subsystems \mathcal{A} and \mathcal{B} .

We take a complete set of operators in the subsystems \mathcal{B} as $\hat{\sigma}_4^\alpha$ (up to a normalization factor), where $\alpha = 0, x, y, z$ and $\hat{\sigma}^0 = \mathbf{1}$. Since $\hat{V} = \hat{O} \hat{O}^\dagger \propto (\mathbf{1} + \hat{\sigma}_1^x)$, the right-hand side of Eq. (5) becomes a set of OTOCs that are given by

$$\langle \hat{\sigma}_4^\alpha(t) (\mathbf{1} + \hat{\sigma}_1^x) \hat{\sigma}_4^\alpha(t) (\mathbf{1} + \hat{\sigma}_1^x) \rangle_{\beta=0}. \quad (6)$$

Notice that $\text{Tr}(\hat{\sigma}_4^\alpha(t) \hat{\sigma}_1^x \hat{\sigma}_4^\alpha(t)) = \text{Tr}(\sigma_4^\alpha(t) \sigma_4^\alpha(t) \sigma_1^x) = 0$, the nonzero terms in Eq. 6 are nothing but OTOCs with $\hat{B} = \sigma_4^\alpha$ ($\alpha = x, y, z$) and $\hat{A} = \sigma_1^x$, which are exactly what we have measured. That is to say, with the help of the relationship between OTOCs and entanglement growth, we can extract the growth of the entanglement entropy after the quench from the experimental data.

The results of 2nd Rényi entropy $S_{\mathcal{A}}^{(2)}$ are shown in

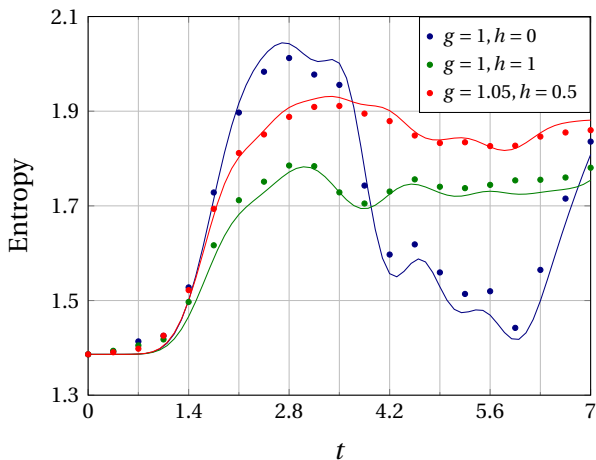


FIG. 3: The 2nd Rényi Entropy $S_{\mathcal{A}}^{(2)}$ after a quench. A quench operator $(\mathbf{1} + \sigma_1^x)$ (up to a normalization factor) is applied to the system at $t = 0$, and the entropy is measured by tracing out the fourth site as the subsystem \mathcal{B} . Different colors correspond to different parameters of g and h in the Ising spin model. The points are experimental data, the curves are theoretical calculations.

Fig. 3. At short time, all three curves start to grow significantly after certain time. This demonstrates that it takes certain time for the perturbation applied at the first site to propagate to the subsystem \mathcal{B} at the fourth site (see the discussion of butterfly velocity below). Then, for all three cases, $S_{\mathcal{A}}^{(2)}$ s grow roughly linearly in time. This indicates that the extra information caused by the initial quench starts to scramble between subsystems \mathcal{A} and \mathcal{B} . The differences lie in the long-time regime. For the integrable model, the $S_{\mathcal{A}}^{(2)}$ oscillates back to around its initial value after some time, which means that this extra information moves back to the subsystem \mathcal{A} around that time window. As a comparison, such a large amplitude oscillation does not occur for the two non-integrable cases and the $S_{\mathcal{A}}^{(2)}$ s saturate after growing. This supports the physical picture that the local information moves around in the integrable model, while it scrambles in the chaotic models [6].

The Butterfly Velocity. The OTOC also provides a tool to determine the speed for correlation propagating. At $t = 0$, \hat{A} and \hat{B} commute with each other since they are operators at different sites. As time grows, the higher order terms in the Baker-Campbell-Hausdorff formula

$$\hat{B}(t) = \sum_{k=0}^{\infty} \frac{(it)^k}{k!} [H, \dots, [H, B], \dots] \quad (7)$$

becomes more and more important and some terms fail to commute with \hat{A} , at which the normalized OTOC starts to drop. Thus, the larger the distance between sites for \hat{A} and \hat{B} , the later time the OTOC starts deviating from

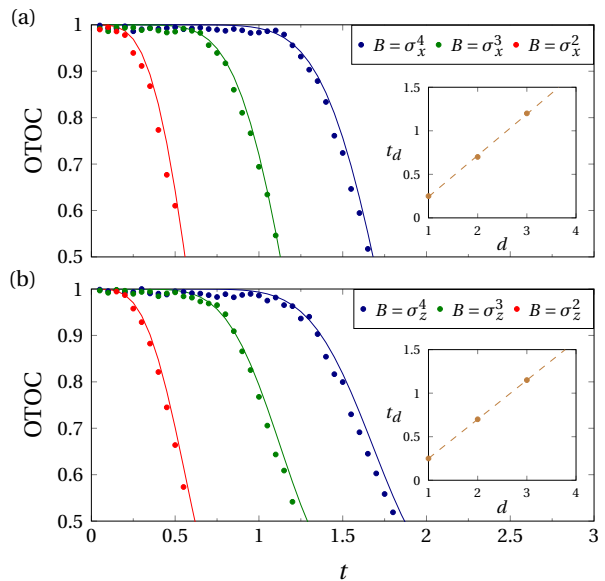


FIG. 4: Measurement of the Butterfly Velocity: (a) shows the OTOCs for $\hat{A} = \sigma_1^z$ and $\hat{B} = \sigma_i^x$ with $i = 4$ (blue), $i = 3$ (green) and $i = 2$ (red); (b) shows the OTOCs for $\hat{A} = \sigma_1^y$ and $\hat{B} = \sigma_i^z$ with $i = 4$ (blue), $i = 3$ (green) and $i = 2$ (red). The insets of (a) and (b) shows the time for the onset of chaos t_d for the OTOCs v.s. the distance between two operators. The slope gives $1/v_B$. Here $g = 1.05$ and $h = 0.5$.

unity. In general, the OTOC behaves as

$$F(t) = a - be^{\lambda_L(t - |x|/v_B)} + \dots, \quad (8)$$

where a and b are two non-universal constants, $|x|$ denotes the distance between two operators. Here v_B defines the butterfly velocity [5, 6, 8–10]. It quantifies the speed of a local operator growth in time and defines a light cone for chaos. It also relates to the Lieb-Robinson bound [10, 42], and the later has been measured in the context of the Bose-Hubbard model [43].

In our experiment, we fix \hat{A} at the first site, and move \hat{B} from the fourth site to the third site, and to the second site. From the experimental data, we can phenomenologically determine a characteristic time t_0 for the onset of chaos in each OTOC, i.e. the time that the OTOC starts departing from unity. By comparing the three different OTOCs in Fig. 4, it is clear that the closer the distance between \hat{A} and \hat{B} , the earlier t_d . In Fig. 4(b) and (d), we plot t_d as a function of the distance, and extract the butterfly velocity from the slope. We find that, for OTOC with $\hat{A} = \sigma_1^z$ and $\hat{B} = \sigma_i^x$, $v_B = 2.10$; and for OTOC with $\hat{A} = \sigma_1^y$ and $\hat{B} = \sigma_i^z$, $v_B = 2.22$. The butterfly velocity is nearly independent of the choice of local operators, which is another manifestation of the chaotic behaviour of the system.

Outlook. Our method opens up possibilities for further experimental measurements of OTOCs on quantum simulators. Together with state preparation, OTOCs

of $\beta \neq 0$ can also be measured, by using an ancilla qubit [29]. In the future it will be interesting to simulate more sophisticated system that processes holographic duality, with larger size and with different β , to extract the corresponding Lyapunov exponents such that one can experimentally verify the connection between the upper bound of the Lyapunov exponent and the holographic duality.

METHODS

Initialization and readout. The system starts at the equilibrium state $\hat{\rho}_{eq} \propto \sum_{i=1}^4 \epsilon_i \hat{\sigma}_i^z$. To measure OTOC, we need to initialise the system at the state $\hat{\rho}_0 \propto A = \sigma_1^\alpha, \alpha = x, y$ or z . We first prepared the system in $\hat{\rho}_0 \propto \hat{\sigma}_1^z$, and other two states $\hat{\sigma}_1^x$ and $\hat{\sigma}_1^y$ can be obtained by a $\frac{\pi}{2}$ pulse along the y or x axis. Because the gyromagnetic ratio of ^{19}F is around four times larger than that of ^{13}C , in order to improve the signal strength of the final measurement, we first prepared the state $\propto \hat{\sigma}_3^z$, and then exchanged the magnetisation from the $^{19}\text{F}_2$ spin to the ^{13}C spin, i.e., $\hat{\rho}_0 \propto \hat{\sigma}_1^z$, by a SWAP gate. The magnetisations of the spins except of F_2 can be saturated by a periodic sequence of on-resonant soft π pulses. The time interval between these π pulses was carefully adjusted so that to good approximation the operator $\hat{\sigma}_3^z$ be the fixed point of the periodic driving. Under such conditions, the system will evolve asymptotically into a steady state ρ_{ss} for which only the $^{19}\text{F}_2$ polarization is retained: $\hat{\rho}_{ss} \approx \mathbf{1}/2^4 + \epsilon_3 \hat{\sigma}_3^z$ (in this sample, we did not see observable Overhauser enhancement). Moreover, the method also saves much time (roughly 10 times speedup) when we repeated the experiments. Thus the system was finally prepared into the state $\hat{\rho}_0 \approx \mathbf{1}/2^4 + \epsilon_3 \hat{\sigma}_1^z$. The term with $\mathbf{1}$ does not effect the final readout of the OTOC except for a scalar factor ϵ_3 : $\langle \hat{O} \rangle_{\beta=0} = \text{Tr}[\rho(t)\hat{A}] = \text{Tr}(\hat{U}(t)\hat{\rho}_0\hat{U}^\dagger(t)\hat{A}) = \epsilon_3 \text{Tr}(\hat{U}(t)\hat{A}\hat{U}^\dagger(t)\hat{A}) = \epsilon_3 F(t)|_{\beta=0}$.

Simulating Ising spin chain and its time-reversal evolution. The many-body system studied is the Ising spin chain of Eq. (2), which is not the same as the natural Hamiltonian of our physical system. If the simulated time-independent Hamiltonian $\hat{H} = \sum_{k=1}^L H_k$, we can then expand the propagator in a symmetric manner as by Trotter formula [33, 34]:

$$e^{-i\hat{H}\tau} = [e^{-i\hat{H}_1\frac{\tau}{2}} e^{-i\hat{H}_2\frac{\tau}{2}} \dots e^{-i\hat{H}_L\frac{\tau}{2}}] \cdot [e^{-i\hat{H}_L\frac{\tau}{2}} e^{-i\hat{H}_{L-1}\frac{\tau}{2}} \dots e^{-i\hat{H}_1\frac{\tau}{2}}] + O(\tau^3), \quad (9)$$

This symmetrization in time makes the expression accurate to second order in τ . If each term H_k can be realized, we can generate the effective Hamiltonian \hat{H} by the right

decomposition. By repeating this period with short evolution times τ , it is then possible to generate arbitrary evolutions. Higher-order decompositions are also possible [44]. Using this method, we write the Ising spin chain as three terms $\hat{H} = \hat{H}_{zz} + \hat{H}_x(g) + \hat{H}_z(h)$, and then we have

$$e^{-i\hat{H}\tau} \approx e^{-i\hat{H}_x\frac{\tau}{2}} e^{-i\hat{H}_z\frac{\tau}{2}} e^{-i\hat{H}_{zz}\tau} e^{-i\hat{H}_z\frac{\tau}{2}} e^{-i\hat{H}_x\frac{\tau}{2}}.$$

Here $e^{-i\hat{H}_x\frac{\tau}{2}}$ and $e^{-i\hat{H}_z\frac{\tau}{2}}$ are the global rotations along x and z axis, and $e^{-i\hat{H}_{zz}\tau}$ is generated by the refocusing pulses (see supplementary information). The whole network is thus constructed by single qubit rotations and time delays. Each local rotation in the circuit is done through a frequency-selective pulse of Gaussian shape. We then conducted a compilation procedure to the sequence of selective pulses to eliminate the control imperfections that are out of off-resonance and coupling effects [45, 46]. After the compilation, the phase errors and unwanted evolutions within the network are compensated up to the first-order dynamics. To further improve the control performance, we used the gradient ascent pulse engineering (GRAPE) technique [47]. Because that compilation procedure has the capability of directly providing a good initial start for subsequent gradient iteration, the GRAPE searching quickly finds out a high performance pulse control for the desired propagators. The obtained shaped pulses for different set of Hamiltonian parameters (g, h) have all the numerical fidelities above 0.999, with practical control field inhomogeneity taken into consideration.

SUPPLEMENTARY INFORMATION

The System Hamiltonian. The precession frequencies and coupling strengths of the system Hamiltonian are given in Fig. 5(a). The relaxation rates of the sample are listed as below

	^{13}C	F_1	F_2	F_3
$T_2^*(s)$	1.22	0.66	0.63	0.61
$T_2(s)$	7.9	4.4	6.8	4.8

Measuring OTOCs. Fig. 5(b) gives the quantum circuit that we are using to simulate the Ising model dynamics and to measure the OTOCs. That is, we irradiate constantly and selectively upon carbon, F_1 and F_3 , so that after sufficiently long time these nuclei are effectively saturated. The key ingredient of the second part is to simulate the Ising Hamiltonian dynamics, for which we have constructed concrete pulse sequences as shown in Fig. 5(c). Choosing different operators for \hat{A} and \hat{B} , we have experimentally measured the corresponding OTO correlator. All the experimental results are given in Fig. 6.

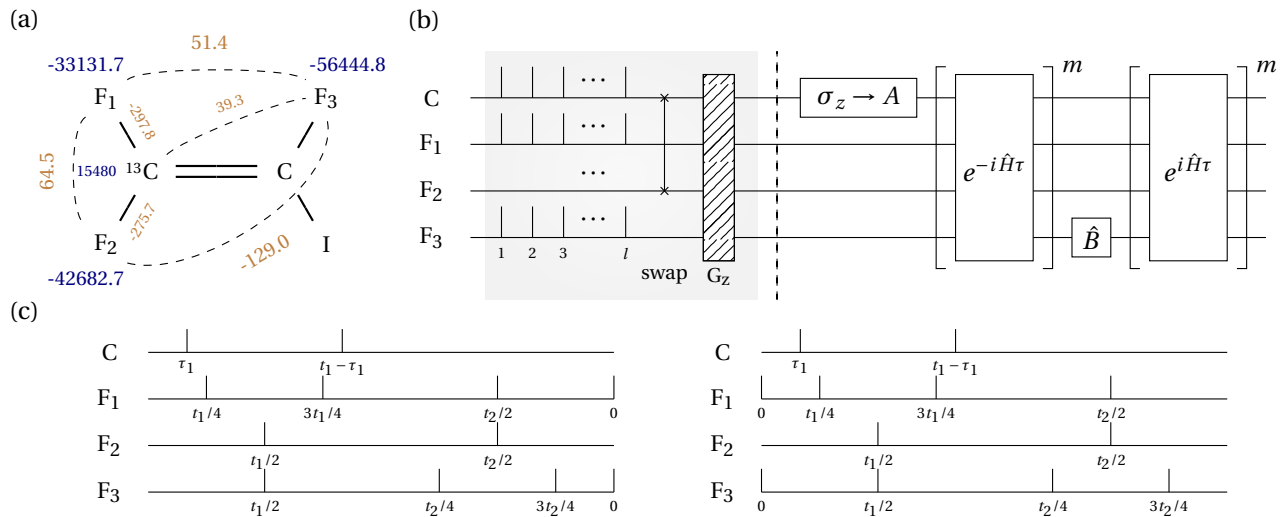


FIG. 5: (a) Iodotrifluoroethylene molecular diagram and its Hamiltonian parameters (all in Hz) experimentally measured on a Bruker AV-400 MHz spectrometer. Blue colored numbers give chemical shifts with respect to the base frequency for ^{13}C or ^{19}F transmitters; brown colored numbers give J coupling terms. (b) Quantum circuit that measures the OTOCs. The black lines represent π pulses. The first part aims at reset an arbitrary state to the desired initial state. Here the distance between the π pulses is 25 ms, the number of cycles is $l = 500$, and G_z denotes z axis gradient pulse. The Ising dynamics to be simulated is discretized into 20 steps, with each time step of duration $\tau = 0.35$ ms. (c) Sequences for implementing the dynamics of $e^{-iH_{zz}\tau}$ (left) and $e^{iH_{zz}\tau}$ (right). The values of the time delays are: $t_1 = 0.004935\tau$, $t_2 = 0.009870\tau$ and $\tau_1 = 0.000534\tau$ so that the refocusing sequences yields the right amount of coupled evolution.

Entanglement Entropy. The the relationship between the growth of 2nd Rényi entropy after a quench and the OTOCs at equilibrium is given in [7], which is stated exhaustively below:

For a system at infinite temperature, we quench it with any operation \hat{O} at $t = 0$. So the density matrix at time t is $\hat{\rho}(t) = e^{-i\hat{H}t}\hat{O}\hat{1}\hat{O}^\dagger e^{i\hat{H}t}$. Then we study the second entanglement Rényi entropy between the subregion \mathcal{B} and the rest is denoted as \mathcal{A} . The reduced density matrix is $\hat{\rho}_{\mathcal{A}}(t) = \text{Tr}_{\mathcal{B}}\hat{\rho}(t)$, which gives us the entropy $S_{\mathcal{A}}^{(2)}(t) = -\log \text{Tr}_{\mathcal{A}}[\hat{\rho}_{\mathcal{A}}(t)^2]$. The growth of entanglement is related to the OTOCs via

$$\exp(-S_{\mathcal{A}}^{(2)}) = \sum_{\hat{M} \in \mathcal{B}} \langle \hat{M}(t)\hat{V}(0)\hat{M}(t)\hat{V}(0) \rangle_{\beta=0}. \quad (10)$$

where the summation is taken over a complete set of operators in \mathcal{B} and $\hat{V} = \hat{O}\hat{O}^\dagger$. Here we should choose the following normalization condition: $\sum_{\hat{M} \in \mathcal{B}} M_{ij}M_{lm} = \delta_{im}\delta_{lj}$, $\text{Tr}[\hat{O}\hat{O}^\dagger] = 1$.

Here, we quench the first site and take the first three sites as the subsystem \mathcal{A} and the fourth site as the subsystem \mathcal{B} , as marked in Fig. 1(b). Hence, we choose $\hat{O} = (1 + \hat{\sigma}_1^x)/2^{(D+1)/2}$ ($D = 4$ is the total number of sites). The complete set of operators in the subsystems \mathcal{B} can be taken as $\hat{\sigma}_4^\alpha/\sqrt{2}$, where $\alpha = 0, x, y, z$ and $\hat{\sigma}^0 = \hat{I}$.

By summing over the measured data with the conventions above, we can get the points in Fig. 3. The theoretical curves are obtained by directly computing entanglement entropy from the density matrix.

* Electronic address: zengb@uoguelph.ca

† Electronic address: hzhai@tsinghua.edu.cn

‡ Electronic address: xhpeng@ustc.edu.cn

- [1] A. Larkin and Y. N. Ovchinnikov, Soviet Journal of Experimental and Theoretical Physics **28**, 1200 (1969).
- [2] A. Kitaev, in *Talk given at the Fundamental Physics Prize Symposium* (2014), vol. 10.
- [3] S. H. Shenker and D. Stanford, Journal of High Energy Physics **2014**, 1 (2014), ISSN 1029-8479, URL [http://dx.doi.org/10.1007/JHEP03\(2014\)067](http://dx.doi.org/10.1007/JHEP03(2014)067).
- [4] S. H. Shenker and D. Stanford, Journal of High Energy Physics **2014**, 1 (2014), ISSN 1029-8479, URL [http://dx.doi.org/10.1007/JHEP12\(2014\)046](http://dx.doi.org/10.1007/JHEP12(2014)046).
- [5] S. H. Shenker and D. Stanford, Journal of High Energy Physics **2015**, 1 (2015), ISSN 1029-8479, URL [http://dx.doi.org/10.1007/JHEP05\(2015\)132](http://dx.doi.org/10.1007/JHEP05(2015)132).
- [6] P. Hosur, X.-L. Qi, D. A. Roberts, and B. Yoshida, Journal of High Energy Physics **2016**, 1 (2016), ISSN 1029-8479, URL [http://dx.doi.org/10.1007/JHEP02\(2016\)004](http://dx.doi.org/10.1007/JHEP02(2016)004).
- [7] R. Fan, P. Zhang, H. Shen, and H. Zhai, arXiv preprint arXiv:1608.01914 (2016).
- [8] D. A. Roberts, D. Stanford, and L. Susskind, Journal of High Energy Physics **2015**, 1 (2015).
- [9] M. Blake, Physical Review Letters **117**, 091601 (2016).
- [10] D. A. Roberts and B. Swingle, Physical Review Letters **117**, 091602 (2016).
- [11] A. Kitaev, talk given at kitp program: *Entanglement in strongly-correlated quantum matter* (2015).
- [12] J. Maldacena, S. H. Shenker, and D. Stanford, arXiv preprint arXiv:1503.01409 (2015).

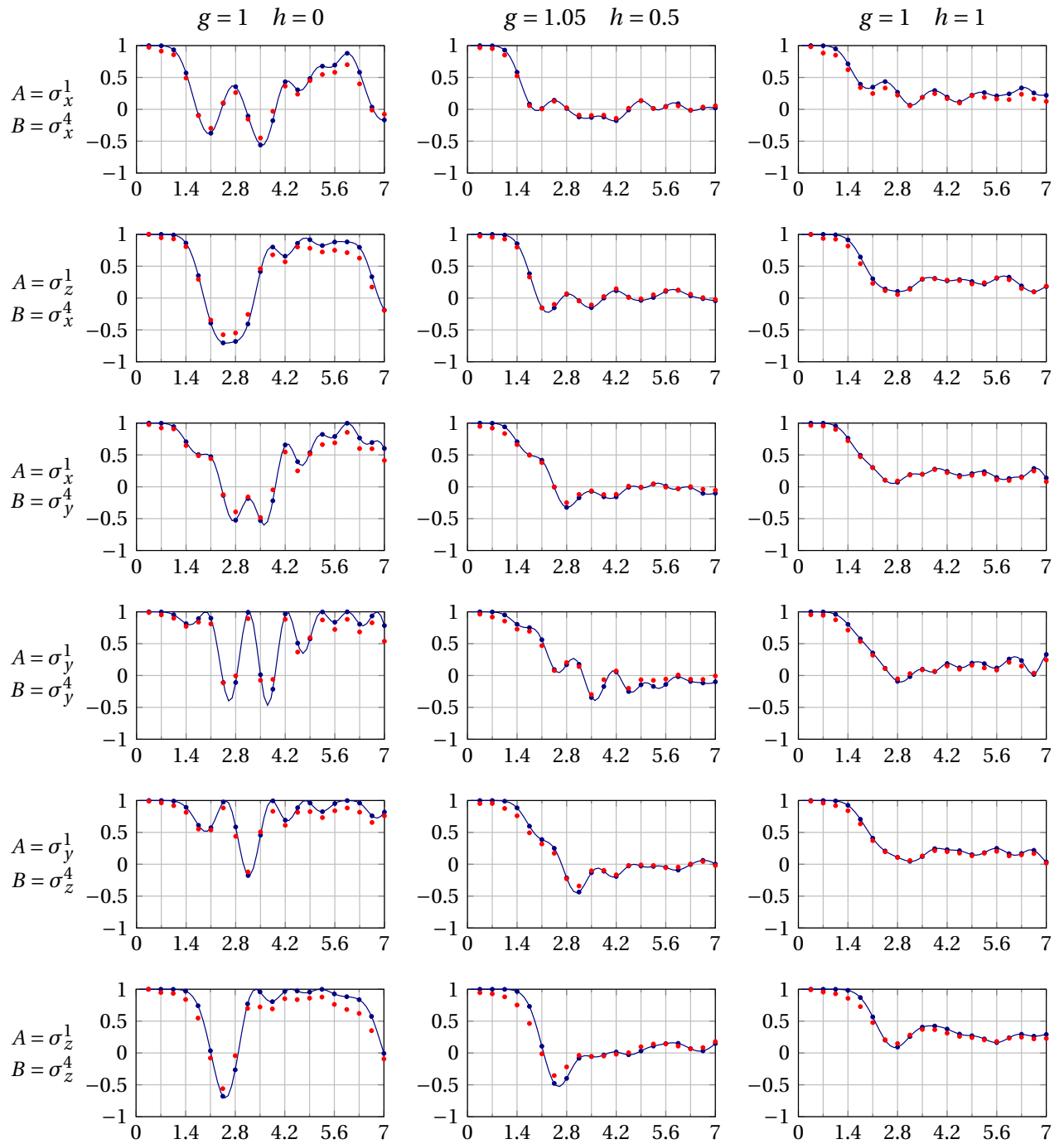


FIG. 6: Experimental results for measuring OTOCs for different Ising model parameters and different pairs of \hat{A} and \hat{B} . The red points are experimental data, the blue curves are theoretical calculation of OTOC with model, the blue points are theoretical values displayed for comparison.

- [13] J. Maldacena and D. Stanford, arXiv preprint arXiv:1604.07818 (2016).
 [14] J. Maldacena, D. Stanford, and Z. Yang, arXiv preprint arXiv:1606.01857 (2016).
 [15] H. Shen, P. Zhang, R. Fan, and H. Zhai, arXiv preprint arXiv:1608.02438 (2016).
 [16] Y. Huang, Y.-L. Zhang, and X. Chen, arXiv preprint arXiv:1608.01091 (2016).
 [17] Y. Chen, arXiv preprint arXiv:1608.02765 (2016).
 [18] B. Swingle and D. Chowdhury, arXiv preprint arXiv:1608.03280 (2016).
 [19] R.-Q. He and Z.-Y. Lu, arXiv preprint arXiv:1608.03586 (2016).
 [20] B. Swingle, G. Bentsen, M. Schleier-Smith, and P. Hayden, arXiv preprint arXiv:1602.06271 (2016).
 [21] G. Zhu, M. Hafezi, and T. Grover, arXiv preprint

- arXiv:1607.00079 (2016).
- [22] N. Y. Yao, F. Grusdt, B. Swingle, M. D. Lukin, D. M. Stamper-Kurn, J. E. Moore, and E. A. Demler, arXiv preprint arXiv:1607.01801 (2016).
- [23] I. Danshita, M. Hanada, and M. Tezuka, arXiv preprint arXiv:1606.02454 (2016).
- [24] L. García-Álvarez, I. Egusquiza, L. Lamata, A. del Campo, J. Sonner, and E. Solano, arXiv preprint arXiv:1607.08560 (2016).
- [25] R. P. Feynman, *International journal of theoretical physics* **21**, 467 (1982).
- [26] R. Somma, G. Ortiz, J. E. Gubernatis, E. Knill, and R. Laflamme, *Physical Review A* **65**, 042323 (2002).
- [27] I. Bloch, J. Dalibard, and S. Nascimbene, *Nature Physics* **8**, 267 (2012).
- [28] R. Blatt and C. Roos, *Nature Physics* **8**, 277 (2012).
- [29] S. Somaroo, C. Tseng, T. Havel, R. Laflamme, and D. G. Cory, *Physical Review Letters* **82**, 5381 (1999).
- [30] X. Peng, Z. Luo, W. Zheng, S. Kou, D. Suter, and J. Du, *Physical Review Letters* **113**, 080404 (2014).
- [31] F. Albertini and D. D'Alessandro, *Linear algebra and its applications* **350**, 213 (2002).
- [32] S. G. Schirmer, H. Fu, and A. I. Solomon, *Physical Review A* **63**, 063410 (2001).
- [33] S. Lloyd, *Science* **273**, 1073 (1996).
- [34] M. A. Nielsen and I. L. Chuang, *Quantum computation and quantum information* (Cambridge university press, 2010).
- [35] B. Zeng, X. Chen, D.-L. Zhou, and X.-G. Wen, arXiv preprint arXiv:1508.02595 (2015).
- [36] D. Lu, T. Xin, N. Yu, Z. Ji, J. Chen, G. Long, J. Baugh, X. Peng, B. Zeng, and R. Laflamme, *Physical Review Letters* **116**, 230501 (2016).
- [37] C. Carmeli, T. Heinosaari, A. Karlsson, J. Schultz, and A. Toigo, *Physical Review Letters* **116**, 230403 (2016).
- [38] O. Gühne and G. Tóth, *Physics Reports* **474**, 1 (2009).
- [39] T. Fukuhara, S. Hild, J. Zeiher, P. Schauß, I. Bloch, M. Endres, and C. Gross, *Physical review letters* **115**, 035302 (2015).
- [40] R. Islam, R. Ma, P. M. Preiss, M. E. Tai, A. Lukin, M. Rispoli, and M. Greiner, *Nature* **528**, 77 (2015).
- [41] H.-N. Dai, B. Yang, A. Reingruber, X.-F. Xu, X. Jiang, Y.-A. Chen, Z.-S. Yuan, and J.-W. Pan, *Nature Physics* (2016).
- [42] E. H. Lieb and D. W. Robinson, in *Statistical Mechanics* (Springer, 1972), pp. 425–431.
- [43] M. Cheneau, P. Barmettler, D. Poletti, M. Endres, P. Schauß, T. Fukuhara, C. Gross, I. Bloch, C. Kollath, and S. Kuhr, *Nature* **481**, 484 (2012).
- [44] M. Suzuki, *Quantum Monte Carlo methods in condensed matter physics* (World Scientific, 1993).
- [45] C. Ryan, C. Negrevergne, M. Laforest, E. Knill, and R. Laflamme, *Physical Review A* **78**, 012328 (2008).
- [46] J. Li, J. Cui, R. Laflamme, and X. Peng, arXiv preprint arXiv:1608.00674 (2016).
- [47] N. Khaneja, T. Reiss, C. Kehlet, T. Schulte-Herbrüggen, and S. J. Glaser, *Journal of Magnetic Resonance* **172**, 296 (2005).
- [48] M. Garttner, J. G. Bohnet, A. Safavi-Naini, M. L. Wall, J. J. Bollinger, and A. M. Rey, arXiv preprint arXiv:1608.08938 (2016).

Notes After finishing this work, we notice a related work [48], where OTOCs are measured in a trapped ion quantum magnet.

Acknowledgements We thank Huitao Shen, Pengfei Zhang, Yingfei Gu and Xie Chen for helpful discussions. B. Z. is supported by NSERC and CIFAR. H. Z. is supported by MOST (grant no. 2016YFA0301604), Tsinghua University Initiative Scientific Research Program, and NSFC Grant No. 11325418. H.W., X.P., and J.D. would like to thank the following funding sources: NKBRP (2013CB921800 and 2014CB848700), the National Science Fund for Distinguished Young Scholars (11425523), NSFC (11375167, 11227901 and 91021005).